

Effects of asymmetrical inflow in forward flight on the deformation of interacting flapping wings

Heitzig, D. N.W.M.; van Oudheusden, B. W.; Olejnik, D.; Karásek, M.

DOI

[10.1177/1756829320941002](https://doi.org/10.1177/1756829320941002)

Publication date

2020

Document Version

Final published version

Published in

International Journal of Micro Air Vehicles

Citation (APA)

Heitzig, D. N. W. M., van Oudheusden, B. W., Olejnik, D., & Karásek, M. (2020). Effects of asymmetrical inflow in forward flight on the deformation of interacting flapping wings. *International Journal of Micro Air Vehicles*, 12. <https://doi.org/10.1177/1756829320941002>

Important note

To cite this publication, please use the final published version (if applicable). Please check the document version above.

Copyright

Other than for strictly personal use, it is not permitted to download, forward or distribute the text or part of it, without the consent of the author(s) and/or copyright holder(s), unless the work is under an open content license such as Creative Commons.

Takedown policy

Please contact us and provide details if you believe this document breaches copyrights. We will remove access to the work immediately and investigate your claim.

Effects of asymmetrical inflow in forward flight on the deformation of interacting flapping wings

International Journal of Micro Air

Vehicles

Volume 12: 1–11

© The Author(s) 2020

Article reuse guidelines:

sagepub.com/journals-permissions

DOI: 10.1177/1756829320941002

journals.sagepub.com/home/mav

DNWM Heitzig , BW van Oudheusden, D Olejnik and M Karásek

Abstract

This study investigates the wing deformation of the DelFly II in forward flight conditions. A measurement setup was developed that maintains adequate viewing axes of the flapping wings for all pitch angles. Recordings of a high-speed camera pair were processed using a point tracking algorithm, allowing 136 points per wing to be measured simultaneously with an estimated accuracy of 0.25 mm. The measurements of forward flight show little change in the typical clap-and-peel motion, suggesting similar effectiveness in all cases. It was found that an air-buffer remains at all times during this phase. The wing rotation and camber reduction during the upstroke suggests low loading during the upstroke in fast forward flight. In slow cases a torsional wave and recoil is found. A study of the isolated effects showed asymmetric deformations even in symmetric freestream conditions. Furthermore, it shows a dominant role of the flapping frequency on the clap-and-peel, while the freestream velocity reduces wing loading outside this phase.

Keywords

Flapping-wing micro air vehicle, wing deformation, fluid–structure interaction, photogrammetry, point tracking

Date received: 5 April 2020; accepted: 25 May 2020

Introduction

Aerodynamic efficiency of flapping-wing fliers was poorly understood until the later part of the 20th century. The low Reynolds number regime in which insects fly should not allow for sufficient lift production to fly. Nonetheless, relatively high lift coefficients are found for hovering insects.¹ Reason for this was later found to be the occurrence of strong leading edge vortices (LEVs), which remain attached to the wing surfaces and delay stall. Especially the “clap-and-fling” mechanism was found to harness this effect strongly,² where LEVs are created between two separating wings.

The wings were thereby assumed to separate rigidly, without any deformation. Subsequent studies however showed that insect wings are highly flexible,³ which further increases efficiency due to passive deformations of the wing shape such as dynamic camber production and wing twisting.⁴ Camber production is thereby assumed to be especially influential, as it delays the LEV detachments, which improves the delayed stall effect.⁵

The present effects occur due to the interaction of aerodynamic and structural, i.e. inertial and elastic,

forces and must therefore be considered in all discussions. Inertial forces acting on the wing trailing edge were, for instance found to result in a phase lag,³ which initiates a recoil effect after stroke reversal that is beneficial to thrust production.⁶ Elastic forces built up over the stroke can lead to extended rotation of the wing trailing edge at the stroke end, while aerodynamic forces act as damping.⁷

In this study, the specific interaction of the flapping-wing micro air vehicle (MAV) “DelFly II,”⁸ henceforth simply called “DelFly,” is investigated. This MAV features two wing pairs in an X-wing configuration, which “clap-and-peel”⁵ on each side. Several studies of the force production⁹ and flow field around the DelFly have already been carried out^{10–12}; however, the wing

Department of Aerospace Engineering, Delft University of Technology, Delft, the Netherlands

Corresponding author:

DNWM Heitzig, Delft University of Technology, Kluyverweg 1, Delft 2629 HS, South Holland, the Netherlands.

Email: dorian.heitzig@me.com



deformation was treated comparatively little.⁷ So far, the deformation was considered to be purely symmetrical, as only a stationary hover case was studied. This study extends this work by introducing a freestream velocity in which the DelFly is pitched to different angles, thus simulating forward flight. This problem is especially interesting, as the clap-and-peel deformation was investigated only very little outside its designed symmetrical condition¹³ and potentially opposing effects such as asymmetrical camber and incidence angle deformations are seen to come into play as fast forward flight is approached.^{4,6}

Experimental setup

The used DelFly MAV (Figure 1) consists of only the X-wing pair with half span, $s_{tip} = 140$ mm; the flapping mechanism enabling stroke angles of $\phi = 44^\circ$; and the electronic speed controller and a central airframe to which it is mounted. Similar to other tethered studies of the DelFly, the tail is omitted, and power is supplied externally using a laboratory power-supply and servo tester to generate the flapping frequency signal. The wing material is chosen to be $15\mu\text{m}$ thick Mylar, together with the default stiffener setup featuring a D-shaped leading edge rod which increases the stiffness in the stroke plane.⁸

Several different optical measurement methods were considered for the measurement of the wing deformation. Ultimately, a back-light point tracking method⁷ was chosen that tracks points applied to the wings over time, which represent the overall wing deformation. Preliminary tests showed that compared to other methods such as digital image correlation¹⁴ or fringe projection,^{15,16} this method can be used to measure both wings simultaneously from one stereo view pair as it does not require opaque wings. Instead, the default transparent DelFly wings can be used, which allows points to be captured through an overlying wing.

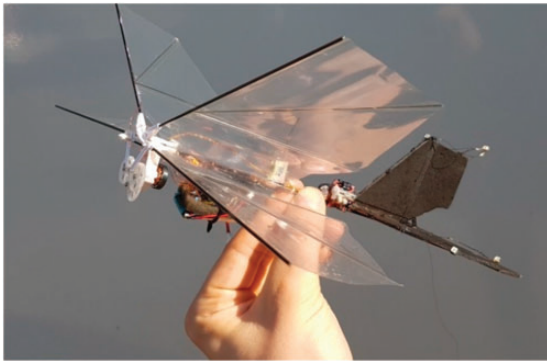


Figure 1. DelFly II MAV in fast forward flight attitude. The used model omits the tail and electronics.¹¹

Measurement setup

The basis of the measurement setup is formed by a frame, which is mounted on a rotating stage positioned below the center of an open $600\text{ mm} \times 600\text{ mm}$ wind-tunnel test section, as shown in Figure 2. The DelFly is mounted on its side, positioned so that the quarter wing chord is exactly over the rotational axis and at 10° pre-pitch relative to the plane of the frame. This proved to give the best optical access through the flapping cycle by the two cameras which are mounted at 10° relative to the frame. The used cameras are two Photron Fastcam SA 1.1 with a CMOS sensor with a $1024\text{ pixel} \times 1024\text{ pixel}$ resolution and $20\mu\text{m}$ pixel pitch capturing at 2 kHz and $1/2000\text{ s}$ exposure. Both are positioned around 600 mm from the DelFly and are fitted with a Nikon lens with 60 mm focal length and $f = 16$ mounted on a Scheimpflug adapter. The background illumination is provided by three LaVision

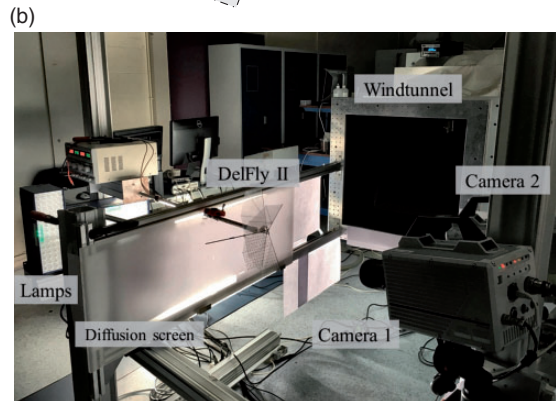
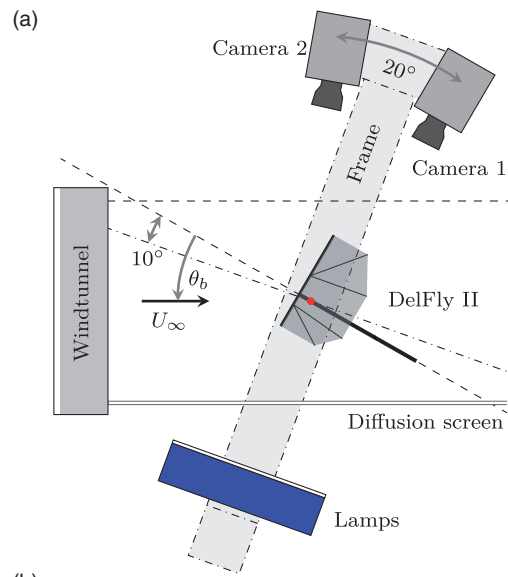


Figure 2. Measurement setup. (a) Top-down sketch on the test section with the DelFly pitched with θ_b around the rotation axis (red) and (b) picture of the measurement setup showing the DelFly mounted in front of the windtunnel nozzle.

LED-Flashlight 300 lamps also mounted to the frame. The lamps are pulsed in sync with the cameras with a 10% duty cycle. Although the lamps produce a relatively large and homogeneous light area, they are further diffused using a combination of a frosted acrylic screen and paper, mounted to the windtunnel nozzle.

This setup allows the pitch angle, θ_b of the DelFly to be adjusted from 0° to 70° by simply manipulating the rotating stage. No readjustments of cameras or lamps are needed to maintain good visibility of the wing deformation, which would require frequent re-calibration. The only exception is that for $\theta_b \geq 50^\circ$ an additional halogen lamp is added on the camera side to provide sufficient illumination of the region close to the windtunnel nozzle.

Per wing, a total of 136 black markers of approximately 1 mm radius are applied using a permanent marker, spaced at around $7.5 \text{ mm} \times 10 \text{ mm}$ as shown in Figure 3. The grids are thereby shifted between the upper and lower wing, so that overlapping of points during the contact phase is avoided. The marker position is exact to approximately 1 mm. This has only very little influence on the measurement process, in theory any arbitrary point spacing may be used.

Point tracking algorithm

The recorded images are processed using a point tracking algorithm coded in MATLAB. Essentially, the algorithm uses a temporal tracking method to follow the image point movements, which are then triangulated to obtain the world locations. As the points are practically indistinguishable, small errors in the exact

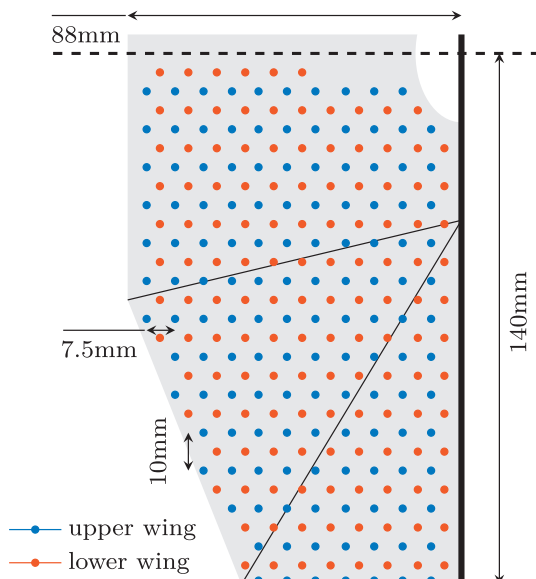


Figure 3. Schematic of DelFly wing half with point grids.

point location can over time lead to larger errors when a point snaps to an incorrect one. This is problematic, especially as the path of points of the two wings often cross. Therefore, the known point spacing is used to reduce noise in the predictions and to detect errors. Once a full flapping cycle is measured, these measurements are used as predictions for the following cycles. This allows the algorithm to run fully automated, with only some initial manual input.

The following paragraphs explain the algorithm in more detail.

Initially, the images recorded in the LaVision software DaVis are imported into MATLAB and pre-processed, which includes distortion correction, background removal using separately recorded images, image inversion, and Gaussian smoothing with a $7 \text{ pixel} \times 7 \text{ pixel}$ kernel size. The camera model necessary for distortion correction and later triangulation is created using the MATLAB stereo camera calibration toolbox.

A two-stage circular Hough transform (CHT) method¹⁷ is used to detect the wing points, starting with a recording where the wings are in contact and almost orthogonal to the camera view. One point per wing must be selected manually, the following will then be detected automatically using the known point spacing and an estimated magnification factor. With all points detected in all views, the stereo calibration is used to calculate the world positions.

For the subsequent timesteps, a temporal tracking method is used to predict the point locations. Therefore, an up to third degree polynomial is fitted to the growing time-series, which coefficients can be used to determine the point velocity components (after the first timestep they are assumed to be zero). The velocity vector multiplied by the timestep then gives an estimation of the point pixel shift. As the determined point locations contain some error, noise quickly accumulates in the determined velocities. Therefore, a spatial fit of the velocities is computed using radial basis interpolation using a C^2 compact support function. If the difference between the calculated and fitted velocity is larger than the velocity fit itself, the fit is used instead of the calculated velocity. The velocities were normalized with the spanwise point location, analogous to the rotational velocity around the stroke axis, to improve the spatial interpolation.

The true point locations are then determined as the simultaneous correspondence between all point predictions and CHT measurements which minimizes the total prediction error. This simultaneous matching of both wings avoids incorrect correspondence of points which easily occurs when points in close proximity are sequentially corresponded. The optimization is done using a mixed-integer linear programming algorithm,

where duplicate use of a measured point is prevented using constraints. If no measurement that fulfills the set tolerance could be found, the point status is set to missing.

These points are neglected in the spatial predictions. Furthermore, in the following timesteps they are corresponded after successfully found points using the world reprojection instead of the temporal prediction. If the point status in one view is considered correct, the prediction in the other view is improved using the epipolar line.

Nonetheless, point correspondences can be incorrect. Therefore, a check for incorrect point measurements is also done in the world domain. Here, a spatial fit of the triangulated points is created using the radial basis interpolation previously used for the in-plane location together with a polynomial fit for the out-of-plane location. Measured point locations, which deviate more than 2.5 mm from the fit, or points that have a reprojection error above 1.5 pixel, are assumed to be incorrectly triangulated.

Once a point exceeds this tolerance by a factor of two, a correction of the triangulation is attempted. For this, the view with lower certainty is selected, which is the view where either no point measurement could be corresponded or where the reprojection of the spatial fit lies further from the measured point location. This incorrect point view is then handled like the missing points described above. The increased tolerance of the correction is used to prevent over-use of corrections without allowing incorrect triangulations to be considered in the spatial predictions.

After a full cycle is measured, the exact cycle length is determined which allows to combine the measurement series to a single cycle. This series is then resampled, thereby filling gaps where points could not be found, to create a prediction for the following cycles. This cyclic prediction is improved with each full cycle as new measurements are added.

The complete measurement series is low-pass filtered using a MATLAB function to remove noise. The cut-off frequency was set to the 10th flapping harmonic, i.e. between 100 and 130 Hz, which is conservative compared to the influence limits found in other studies.^{18,19}

Method verification and accuracy

The described algorithm works well in determining the DelFly wing deformation. On average, the reprojection error lies at around 0.21 pixel with 3.4% point tracks are determined to be incorrect based on the mentioned criteria. The tracking quality is thereby lower for the second cycle half and the lower wing as point motions are possibly less favorable and larger points are more often occluded by stiffeners. Worse tracking results in

isolated false positive point measurements, which increase the mean reprojection error.

Measurements of a 150 mm diameter reference sphere were done to get a better understanding of the general setup accuracy. The 63 markers of 1 mm radius had an average reprojection error of 0.11 pixel and could be fit to a sphere with a standard deviation of 0.13 mm. Assuming a linear relation with the reprojection error, the deformation measurements can be said to be accurate to approximately 0.25 mm.

Airfoil parameter definition

The following discussion uses the measured points to represent the wing surface, i.e. the most forward and backward points are used as wing leading and trailing edge, respectively. To obtain equivalent parameters, the points on the lower wing are interpolated to match the upper wing. The total of 2000 measurements is allocated to 100 phase bins over the flapping cycle to calculate the deformation statistics. The phase is thereby indicated by the non-dimensionalized time, $t^* = t/T$, where period, $T = 1/f$, with $t^* = 0$ at the closest distance between the wing leading edges. Thus, the cycle starts with the outstroke and ends with the instroke.

The point measurements are transferred from the body coordinate system to a wing coordinate system fixed to the wing leading edge shown in Figure 4(a). An exemplary $x_w - z_w$ cut at span location s_w is shown in Figure 4(b). In this plot, the shown measurements are normalized by the mean chord, $c_{mean} = 80$ mm, indicated by the asterisk and the origin is shifted by $\Delta z_w = \tan(\phi)s_w$ to the intersection with the dihedral plane to visualize the stroke angle.⁷

The wing coordinate system is also used to calculate different local wing airfoil parameters. The camber ratio, ε is the ratio between the airfoil camber and chord, where a airfoil curvature against z_w -direction is defined as negative. The incidence angle, θ_w is the angle between the chordline and the x_w -axis and used to describe wing twisting. θ_w is also linked to the delay between the leading and trailing edge stroke. The difference between incidence angle and angle of the inflow velocity, $U_{tot,w}$ is used to represent the angle of attack, α . The inflow direction is thereby calculated from the sum of the freestream velocity in the wing reference frame, $U_{\infty,w}$ and the leading edge velocity, $U_{LE,w}$. Induced velocities are neglected.

Wing deformation in forward flight

Horizontal forward flight of the DelFly is achieved by pitching the MAV forward. This results in a horizontal component of the forces produced by the flapping

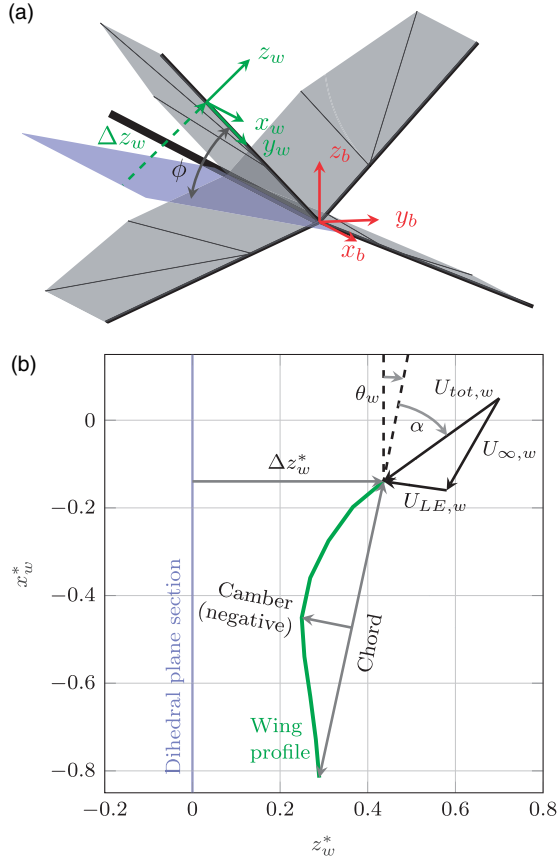


Figure 4. Used coordinate systems. (a) Sketch of the DelFly including body (red) and local wing (green) coordinate systems and dihedral plane (blue) and (b) definition of wing airfoil parameters in normalized $x_w^*-z_w^*$ plane at spanwise location s_w .

wings, which typically act in x_b -direction due to the wing symmetry. To maintain a specific altitude, the flapping frequency must then be matched to the pitch angle. Each θ_b then results in a certain forward velocity. To simulate this in the windtunnel, the parameters θ_b , f , and U_∞ were set to replicate values measured in previous free forward flight investigations.^{9,12} The cases investigated here are shown in Table 1. The Reynolds number, based on freestream velocity and mean wing chord, varies between $Re \approx 2600$ and 12,000 for these cases.

General wing deformation

A representation of the temporal development of the wing deformation is given in Figure 5. The spanwise location, $s_w = 100 \text{ mm} = 0.71 s_{tip}$ is chosen as it gives a good representation of the entire wing shape. In spanwise direction the deformation is relatively straightforward, where the deformation magnitude typically increases toward the wing tips while maintaining the same temporal trends.

Table 1. Tethered flight settings representing free forward flight.

θ_b ($^\circ$)	U_∞ (m s^{-1})	$U_{\infty,z}$ (m s^{-1})	f (Hz)
70	0.50	0.47	13.00
50	1.12	0.85	11.89
40	1.63	1.05	11.07
30	2.26	1.13	10.11

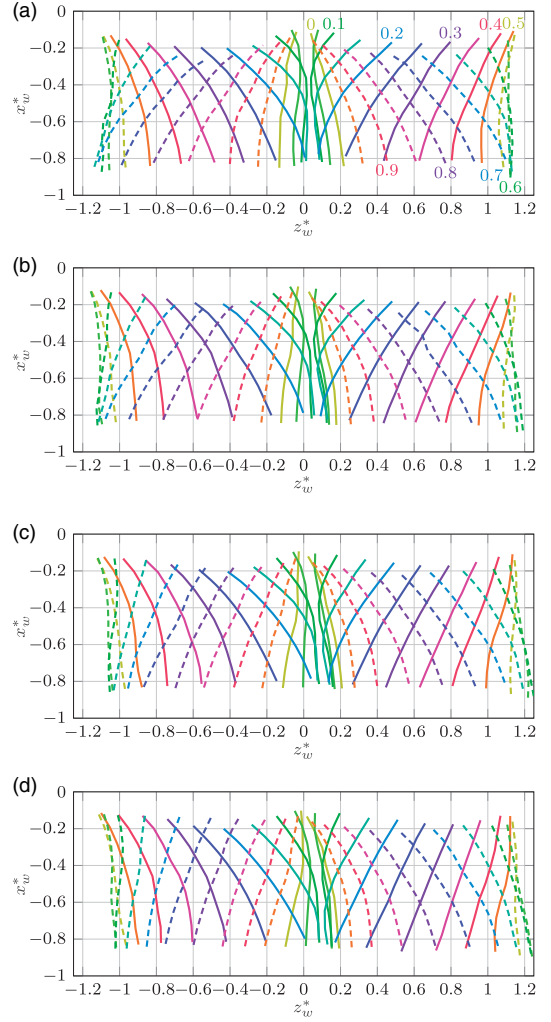


Figure 5. Wing airfoil deformation at $0.71 s_{tip}$ over the flapping cycle due to different forward flight velocities. The upper wing can be seen in the right half, the instroke airfoils are dashed. (a) 0.5 m s^{-1} forward flight at $\theta_b = 70^\circ$. t^* is indicated for the upper wing, (b) 1.12 m s^{-1} forward flight at $\theta_b = 50^\circ$, (c) 1.63 m s^{-1} forward flight at $\theta_b = 40^\circ$, and (d) 2.26 m s^{-1} forward flight at $\theta_b = 30^\circ$.

The characteristic clap-and-peel motion can be seen in Figure 5(a), where between $t^* = 0$ and $t^* \approx 0.2$ the two wings rolling-off on each other, which produces a large camber. It was already found that leading edges

thereby make no contact.⁷ However now, thanks to the simultaneous measurements of both wings, it can be seen that also the remaining wing surfaces do not come in contact, oppositely to what was previously assumed. Only in small regions around the root trailing edge and wing stiffeners the wings appear to make contact. The general presence of this air-buffer between the wing surfaces is plausible, as viscous forces prevent large fluid accelerations close to the wing surfaces. This gap is likely increased further due to the interaction of pressure fields and elastic forces over the flapping cycle. Measurements show that the mean minimum gap along the chord at $s_w = 0.71 s_{tip}$ increases slightly from around $\Delta z_{CNP} = 2.4$ to 2.7 mm between the slowest and fastest forward flight case. Thereby, the clap-and-peel duration reduces slightly from $\Delta t_{CNP}^* = 0.187$ to 0.171 at this spanwise location.

Apart from this, in all cases a mean incidence angle directed toward the freestream direction is clearly present. Also, it can be seen that airfoils flatten as they move in positive while camber increases during movement in negative direction. To better describe the movement relative to the axis and freestream direction, the terms up- and downstroke are introduced. These correspond inversely to in- and outstroke for the upper and lower wing. Especially in fast forward flight the airfoil deformation relates mostly to the up- and downstroke. The predominantly flat airfoils during the upstroke (left to right movement) in Figure 5(d) show this clearly. A good indication of the asymmetric deformation is the freestream component in z_w direction, $U_{\infty,z} = \sin(\theta_b) U_{\infty}$ (listed in Table 1) is a better measure, which is representative of the larger out-of-plane component of the lift vector.

Interesting to see is that the core clap-and-peel deformation remains relatively unaffected by the pitch angle and appears to be simply rotated to a twisted wing contact plane. Due to this rotation, the leading edge path of the lower wing (shown on the left) is directed considerably more backwards, which results in an asymmetric heave of both wings. The wings are heaving more during the downstroke, which typically indicates higher loads during this phase.

Airfoil parameters

The wing airfoil parameter plots shown in Figure 6 give further insight into the deformations.

As seen before, the incidence angle peaks around the middle of each stroke for all cases. In the outstroke phase, the peak occurs at the end of the clap-and-peel, when the trailing edges detach. This is followed by a rapid acceleration of the trailing edges, which quickly exceed the leading edge velocity and thus reduces the incidence angle. The large acceleration is

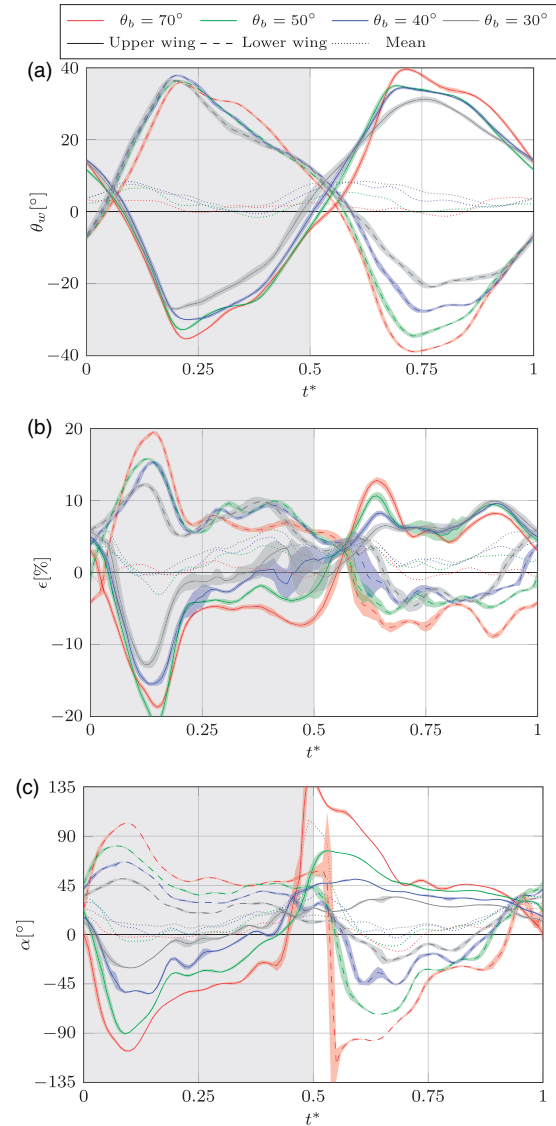


Figure 6. Wing airfoil parameters at $0.71 s_{tip}$ due to different forward flight velocities, indicated by θ_b . The outstroke phase is shaded in gray, the instantaneous s.d. is shaded, respectively. (a) Incidence angle, (b) camber ratio, and (c) angle of attack.

likely due to the elastic forces build-up during the clap-and-peel phase.

In all cases, the mean incidence angle of the two wings is positive over most of the cycle, especially for the cases with a large normal freestream component. This is especially prominent during stroke reversal, where the inflow velocity is almost entirely made up by the freestream velocity. The positive mean occurs also as the incidence during the upstroke (negative θ_w) varies more with the pitch angle, especially during the instroke.

Small variations of the incidence angle during the clap-and-peel phase show that this phase is relatively

unaffected by the asymmetric inflow. The only difference is a small shift in the initial incidence angle, which was seen as a rotation of the symmetry plane, while the rate of incidence angle increase remains identical.

The assumption that the clap-and-peel behavior is largely unaffected is also supported by the measured camber deformation. While initially both wings have positive camber ratios, between $t^* = 0.05$ and $t^* = 0.18$ the camber ratio is almost symmetric. The $\theta_b = 50^\circ$ case is the only outlier for this assumption. It appears that here due to the specific contact region rotation a sharper peel-off angle results in a larger camber production.

Larger asymmetries occur outside the clap-and-peel phase. During the downstroke similar positive camber ratios occur for all cases; however, during the upstroke the camber ratio reduces approximately proportional to the pitch angle, approaching zero for the $\theta_b = 30^\circ$ case. This wing flattening has also been found in forward flight of insects.^{4,6}

Looking closely at the airfoil shape in Figure 5(d), it shows that here the upper wing has an S-shape toward the end of the upstroke. At the leading edge the airfoil is already curved upwards, while the trailing edge is still curved downwards. Toward the wing tip this behavior is increased where the entire airfoil inverts already before the stroke reversal. The developing S-shape makes the determination of the camber direction difficult, which leads to large s.d. in this instance.

This phenomenon can be better understood when considering the wing loading, which can be estimated using the calculated angle of attack given in Figure 6 (c). While α remains mostly constant during the downstroke, α approaches zero during the upstroke in fast forward flight. This reduction occurs as the wing moves in direction of the freestream velocity, minimizing the incidence angle and relative velocity during the upstroke.¹⁹ In fact, the sign change of α coincides almost exactly with that of ε for cases where $\theta_b \leq 40^\circ$. This is remarkable, especially considering the neglect of induced velocities and the likely presence of structural effects. The reversal of camber and inflow direction suggests that produced forces are also reversed and start to act upwards, even before the downstroke commences. This effectively increases the duration of lift production, while reducing thrust production, a phenomenon which is also assumed to occur for single wing insects.⁴

Apart from this, the angle of attack further strengthens the assumption that the clap-and-peel phase remains a symmetric phenomenon, as the lower and upper wing show a similarly large angle of attack. Large angles of attack above 45° in all cases indicate the production of LEVs, even in the fastest forward

flight case. Together with the alignment of the clap-and-peel motion with the flight direction, this suggests a major part of the required thrust is being produced in this phase.

The large spike in α at the outer stroke reversal of the $\theta_b = 70^\circ$ case occurs due to small changes in the leading edge movement direction while the freestream component is minimal. Therefore, produced loading is also minor and can be neglected.

Individual parameter study

As the MAV is tethered in a windtunnel, the effects of changing f , U_∞ , and θ_b can be investigated individually. It will show that a simple superposition of the individual effects does not fully align with the deformation in true forward flight. This is expected, as the wing deformation is generally considered to be non-linear. Nonetheless, the results allow some further insight to deformation in flapping-wing flight.

Varying flapping frequency in steady ambient conditions

The influence of flapping frequency variation has already been investigated in studies of the Delfly in tethered hovering flight.⁷ It was found that an increasing flapping frequency at zero freestream velocity results in a large increase in the incidence angle, heaving motion, and camber production. Also, the trailing edge stroke is reduced and delayed in phase. These effects are linked to an increased wing loading due to the faster motion which outweighs the reduction of angle of attack in these cases. Thereby, the camber increases especially during the clap-and-peel phase. The new measurements agree closely with these findings.

As now both the lower and upper wing are measured, some additional findings could be made. For the forward flight case a presence of a gap between both wing surfaces was already noted. This phenomenon also occurs in the zero-freestream case. Between

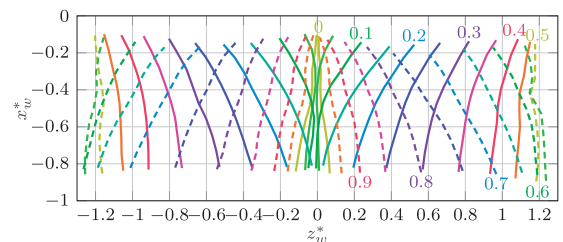


Figure 7. Asymmetric wing deformation in static ambient condition at $f = 7.5$ Hz, represented by the airfoil at $0.71 s_{tip}$. The upper wing is shown in the right half, the instroke is dashed.

the measured cases of $f=7.5$ and 12 Hz, the mean gap doubles from $-\Delta z_{CNP}=0.8$ to 1.6 mm, while the clap-and-peel duration increases from $\Delta t_{CNP}^*=0.136$ to 0.174.

Furthermore, the results show asymmetries between the deformation of the lower and upper wing, while previously the deformation was assumed to be purely symmetrical in steady ambient conditions. This asymmetry is clearly visible in Figure 7, for instance during the end of the outstroke, where the lower wing displays camber while the upper wing is mostly flat. Also, the leading edge of the upper wing heaves considerably more during the instroke, while the lower wing heaves approximately identically in both stroke directions.

A main reason for this asymmetry can be seen in the dihedral angle of the DelFly. This results in the upper wing tips coming closer to each other compared to the lower wings. This will lead to minor differences in the aerodynamic behavior, as well as asymmetric wing tensioning. Inaccuracies in the manual manufacturing process of the wings may increase this effect and further discrepancies may be introduced by the support and diffusion wall.

Careful study of the spanwise wing deformation showed a torsional wave travelling along the span of the upper wing, which increases the incidence angle quickly at the start of the instroke. A 3D animation of this motion is shown in Video 1 (https://www.youtube.com/playlist?list=PL_KSX9GOn2P-hxC4vUo07Kg7u8V8tOBkE). This spanwise variation is also seen in other flapping-wing fliers.¹³ At $f=12$ Hz a rapid increase in camber also occurs at the same, which is again found in insect flight.^{3,6} This recoil effect is linked to inertial forces which lead to a trailing edge lag and has been found to increase thrust production. Looking back at Figure 6, these effects can also be seen at the start of the instroke of the upper wing at slow forward flight, where θ_w and ε increase very rapidly. In faster forward flight this motion is no longer seen: This may be a result of the advanced lift production of the upper wing.

Varying symmetric freestream velocity

Next, the effect of increasing freestream velocity aligned with the airframe was investigated. The symmetric external flow approximates vertical climbing flight, a state that is not achievable with the DelFly II as it requires additional flow over the tail to maintain stability. However, a tailless variation of the DelFly that has been developed recently can sustain such condition more reliably,²⁰ making the case of further interest.

Table 2. Variation of wing deformation parameters at 0.71 s_{tip} due to different freestream velocities.

U_∞ ($m s^{-1}$)	$\overline{\Delta z_{CNP}}$ (mm)	Δt_{CNP}^* (-)	$\left(\frac{\Delta \varepsilon}{2}\right)_{max}$ (%)	$\left(\frac{\Delta \theta_w}{2}\right)_{out, max}$ ($^\circ$)	$\left(\frac{\Delta \theta_w}{2}\right)_{in, max}$ ($^\circ$)
0.0	1.6	0.174	17.4	33.6	36.1
1.0	1.8	0.186	17.4	33.6	34.8
2.0	2.3	0.193	14.8	34.3	31.1

Key wing deformation parameters at different U_∞ are given in Table 2, where f and θ_b kept at 12 Hz and 0° , respectively. Asymmetries between the lower and upper wing are reduced as the freestream velocity increases. To neglect them in the airfoil parameters, half the delta between the lower and upper wing are taken. For instance, for the camber $(\Delta \varepsilon/2)_{max}$.

Increasing the freestream velocity from $U_\infty=0$ to $2 m s^{-1}$ results in a mean gap increase of 44%. The duration of the clap-and-peel motion increases also with the freestream velocity. The slower detachment of the leading edges together with a larger wing surface distance appears to reduce the initial peak in camber for the fastest freestream case. Thus, the change can be mostly linked to a structural effect, while large angle of attack above 45° suggests strong LEVs in all cases. Outside the clap-and-peel case the camber ratio is however more significantly affected by the increased freestream velocity.

During the clap-and-peel, the incidence angle also shows little variation due to the changing freestream velocity, as it increases and peaks almost identically for all cases. Also during the remaining outstroke, the incidence angle shows little variation, which is likely due to the release of stored elastic forces. Only a minor phase delay in the incidence angle can be seen, similar to that found in the hover case.⁷ Here, this delay can be linked to a larger stroke angle of the leading edge during the hover case, while the trailing edge stroke remains almost identical.

Compared to this, the incidence angle during the instroke varies considerably more, with $(\theta_w/2)_{in, max}$ reduced by 5° for the fastest freestream velocity. Similarly, to the hover case, this can again be attributed to a reduced wing loading. As the freestream component is increased, the inflow angle reduces quickly. For $U_\infty=2 m s^{-1}$ this results in an angle of attack of $|\alpha| \approx 20^\circ$ during the majority of the fast stroke phases. This holds for most of the wing, only at the wing tip larger angles are found. The reduction of α outweighs the inflow velocity increase, therefore leading to lower

aerodynamic forces which reduces incidence angles and increases the stroke.

The combination of flapping frequency and free-stream velocity variation is often described by the reduced frequency, k . The limited test cases show that the deformation does not scale well with this parameter, as variations in f typically dominate variations in U_∞ . Only α increases steadily with k in all tested cases.

This becomes evident when adding the individual effects of f and U_∞ to represent forward flight. The peak incidence angle during the outstroke reduces by 3.8° between the fastest and slowest forward flight case, compared to a calculated 5° reduction of the superposition. During the outstroke, this discrepancy becomes even larger with 13° compared to a 9.4° reduction. The camber during the clap-and-peel however scales relatively well. In free forward flight, a 5.5% percent reduction occurs between the slowest and fastest case, while the superposition of f and U_∞ accounts for a 3 and 2.3% reduction, respectively.

Varying pitch angle

Lastly, the effect of varying pitch angle was studied. The measured cases are shown in Table 3, where $f=12$ Hz and $U_\infty = 1$ m s⁻¹. As the pitch angle introduces a larger asymmetry, the asymmetric effects are now of main interest. Mathematically, this is represented by the mean of the upper and lower wing, indicated by the bar above the respective variable.

The camber ratio shows asymmetries especially during the fast stroke phases, where at larger pitch angles the camber is increased during the downstroke while the wing flattens during the upstroke. During the clap-and-peel the effect is actually inverse, which is likely due to the alignment of the symmetry plane with the inflow motion, as already noted in forward flight. In general, the asymmetric camber effects align quite well with coupled forward flight; also the limited recoil effect is visible in the upper wing.

The mean incidence angle also increases at larger normal freestream velocities, as it was the case in forward flight. Magnitudes are comparable; however, here these peaks occur only around the stroke reversal,

compared to a more constant positive mean incidence angle in forward flight. This is likely due to the coupling with the changing flapping frequency and free-stream component, where the delta in incidence angle already showed to scale poorly.

Interestingly, the increased asymmetry also has a large influence on the clap-and-peel wing gap. The 0.9 mm difference between the $\theta_b = 30^\circ$ and 70° case is considerably larger than the 0.3 mm increase between the respective forward flight case, which suggests further interactions with the remaining effects. The clap-and-peel duration meanwhile remains almost constant.

Conclusion

An optical measurement setup was developed which co-aligns the tethered DelFly with a camera pair and background light. This allows to maintain adequate viewing axes of the wings as they undergo large stroke angles. As the wings are transparent, 136 points applied to each wing could be measured simultaneously. The points were tracked using a purpose-built point tracking algorithm, which uses known structural information to enhance the temporal tracking so that false point matches are mostly avoided. The general accuracy lies around 0.25 mm based on reference sphere measurements. The developed setup and measurement algorithm may be useful in the future for investigating different flight states or other models and may also be an important tool for optimizing wing designs and generating validation data for numeric methods.

Using the developed measurement setup, the DelFly wing deformations were measured in simulated free flight conditions. The measurements show behaviors which to the best of our knowledge have not yet been noted in literature on interacting flapping wings. First, measurements show that the wing surfaces do not touch during the clap-and-peel phase, instead an air-buffer remains at all times. Along the chord at 0.71 s_{tip} spanwise position, the surfaces have a mean air-buffer of around 2.5 mm, which increases with forward flight velocity. Furthermore, slight asymmetries are found even in symmetrical inflow conditions. To an extent these are inherent because of the dihedral angle, which influences aerodynamics and wing tension, but may also be a result of measurement uncertainties.

The forward flight study shows that asymmetries are especially large in fast forward flight. The clap-and-peel by itself is thereby mostly unaffected, most noticeable is only the rotation of the symmetry plane to align with the inflow direction. This indicates that the produced LEV has a dominant effect over the asymmetrical free-stream velocity and that the flapping motion likely remains as effective as in hover. Outside the clap-and-peel a positive mean incidence angle and camber ratio

Table 3. Variation of wing deformation parameters at 0.71 s_{tip} due to different pitch angles.

θ_b ($^\circ$)	$U_{\infty,z}$ (m s ⁻¹)	$\overline{\Delta z_{CNP}}$ (mm)	Δt_{CNP}^* (-)	$\overline{\theta}_{w_{max}}^{out}$ ($^\circ$)	$\overline{\theta}_{w_{max}}^{in}$ ($^\circ$)
0	0.00	1.8	0.186	2.14	2.60
30	0.50	2.0	0.187	3.58	3.12
50	0.77	2.3	0.186	5.99	4.88
70	0.94	2.9	0.187	9.21	4.47

is present. Especially during the upstroke the incidence angle and camber are reduced. This indicates reduced wing loading, which is also supported by the measured angle of attack and is also common in insect flight.^{4,6} For slow forward flight, a recoil and torsional wave motion was noted to occur at the start of the instroke of the upper wing.

Additionally, the individual effects of varying flapping frequency, freestream velocity, and pitch angle were studied. The results strengthen the assumption of non-linear effects, as superposition of the individual effects showed to represent coupled forward flight only poorly. To an extent, the deformation during clap-and-peel appears to be an exception, as it is strongly coupled to the flapping frequency. Apart from the clap-and-peel, the freestream velocity shows a larger influence on the camber and incidence angle. While the release of elastic energy stored in the clap-and-peel phase still shows an impact, the reduced aerodynamic wing loading due to lower inflow angles drives the reduction in incidence angles and camber ratios. The pitch angle meanwhile affects the mean incidence angles and camber of both wings. However, the magnitude is considerably different from the forward flight and is also limited to shorter durations around the stroke reversals. Furthermore, the isolated study also proved that the wing deformation is asymmetric even in steady ambient conditions. Additional studies should be done to understand the absence of the recoil effect in the lower wing. Modifying the design to obtain the same effects as in the upper wing may allow to increase the thrust production in slow forward flight further.

Generally, the carried out measurements give a more detailed description of wing deformation in flight of interacting flapping wings which may drive better understanding and design of MAVs in the future.

Declaration of conflicting interests

The author(s) declared no potential conflicts of interest with respect to the research, authorship, and/or publication of this article.

Funding

The author(s) received no financial support for the research, authorship, and/or publication of this article.

ORCID iD

DNWM Heitzig  <https://orcid.org/0000-0001-9484-907X>

References

- Jones AR and Babinsky H. Unsteady lift generation on rotating wings at low Reynolds numbers. *J Aircraft* 2010; 47: 1013–1021.
- Weis-Fogh T. Quick estimates of flight fitness in hovering animals, including novel mechanisms for lift production. *J Exp Biol* 1973; 59: 169–230.
- Ellington CP. The aerodynamics of hovering insect flight. III. Kinematics. *Phil Trans R Soc B Biol Sci* 1984; 305: 41–78.
- Wang H. Measuring wing kinematics, flight trajectory and body attitude during forward flight and turning maneuvers in dragonflies. *J Aircraft* 2003; 206: 745–757.
- Du G and Sun M. Effects of unsteady deformation of flapping wing on its aerodynamic forces. *Appl Math Mech* 2008; 29: 731–743.
- Walker SM, Thomas ALR and Taylor GK. Deformable wing kinematics in free-flying hoverflies. *J R Soc Interface* 2010; 7: 131–142.
- Perçin M, van Oudheusden BW, De Croon GCHE, et al. Force generation and wing deformation characteristics of a flapping-wing micro air vehicle ‘DeIFly II’ in hovering flight. *Bioinspir Biomim* 2016; 11: 036014.
- De Croon GCHE, Perçin M, Remes B, et al. *The DeIFly: design, aerodynamics, and artificial intelligence of a flapping wing robot*. Dordrecht: Springer Netherlands, 2016.
- Karásek M, Koopmans AJ, Armanini SF, et al. Free flight force estimation of a 23.5 g flapping wing MAV using an on-board IMU. In: *Proceedings of the 2016 IEEE/RSJ international conference on intelligent robots and systems (IROS)*, Daejeon, South Korea, 2016, pp.4963–4969. DOI: 10.1109/IROS.2016.7759729
- Perçin M, van Oudheusden BW, Eisma HE, et al. Three-dimensional vortex wake structure of a flapping-wing micro aerial vehicle in forward flight configuration. *Exp Fluids* 2014; 55: 729.
- del Estal Herrero A, Percin M, Karasek M, et al. Flow visualization around a flapping-wing micro air vehicle in free flight using large-scale PIV. *Aerospace* 2018; 5: 99.
- Martínez Gallar B, van Oudheusden BW, Sciacchitano A, et al. Large-scale flow visualization of a flapping-wing micro air vehicle. In: *Proceedings 18th international symposium on flow visualization*, 2018.
- Nakata T, Liu H, Tanaka Y, et al. Aerodynamics of a bio-inspired flexible flapping-wing micro air vehicle. *Bioinspir Biomim* 2011; 6: 045002.
- Wu P, Stanford B, Bowman W, et al. Digital image correlation techniques for full-field displacement measurements of micro air vehicle flapping wings. *Exp Tech* 2009; 3: 53–58.
- Song D, Wang H, Zeng L, et al. Measuring the camber deformation of a dragonfly wing using projected comb fringe. *Rev Sci Instrum* 2001; 72: 2450–2454.
- Li B and Zhang S. Superfast high-resolution absolute 3D recovery of a stabilized flapping flight process. *Optics Express* 2017; 25: 27270–27282.
- Yuen HK, Princen J, Illingworth J, et al. Comparative study of Hough transform methods for circle finding. *Image Vision Comput* 1990; 8: 71–77.
- Walker SM, Thomas ALR and Taylor GK. Photogrammetric reconstruction of high-resolution

- surface topographies and deformable wing kinematics of tethered locusts and free-flying hoverflies. *J R Soc Interface* 2009; 6: 351–366.
19. Deng S. *Aerodynamics of flapping-wing micro-air-vehicle*. PhD Thesis, Technische Universiteit Delft, Netherlands, 2016.
 20. Karásek M, Muijres FT, De Wagter C, et al. A tailless aerial robotic flapper reveals that flies use torque coupling in rapid banked turns. *Science* 2018; 361: 1089–1094.